Twenty-Seventh Symposium (International) on Combustion/The Combustion Institute, 1998/pp. 2635–2641

DIMENSIONAL EFFECTS ON THE TRANSITION FROM IGNITION TO FLAME SPREAD IN MICROGRAVITY

W. E. MELL AND T. KASHIWAGI
National Institute of Standards and Technology
Gaithersburg, Maryland 20899-0001, USA

Three-dimensional (3-D) and two-dimensional (2-D) simulations of the transition from radiative ignition on a solid fuel to flame spread in an imposed wind were performed in microgravity. Two-dimensional flames were found to quench (due to poor oxygen supply) more easily (i.e., at larger wind speeds) than 3-D flames. Results from the 2- and 3-D simulations were compared during the transition phase at wind speeds that ultimately lead to quenching of the 2-D flame but survival of the 3-D flame. In all locations near and in the flame, oxygen mass flux was larger in the 3-D flames and dominated by diffusion (as opposed to convection). Oxygen was supplied to the core of the 3-D flame due to diffusion from the sides of the flame (in a cross-wind direction). Diffusion in the 2-D flame was limited to directions parallel to the wind. This cross-wind diffusion was most significant at early times during transition when the flame was small and had a relatively large curvature. The 3-D flame, therefore, required less oxygen supply from an external wind to undergo transition to flame spread. Once flame spread was established there was little difference between the 3-D flames (in the centerline plane) and 2-D flames, due to the decreased curvature of the three-dimensional flame relative to the curvature during ignition and transition.

Introduction

The process of transition in which a flame on a solid fuel passes from ignition to established flame spread is of scientific interest and also has fire safety applications. For example, in a human-occupied spacecraft, ignition followed shortly by extinction could result in conditions that remain within safety limits. However, if transition to flame spread occurs, crew safety could be jeopardized. Determining the limiting conditions under which successful transition to flame spread occurs requires a model that simulates the processes involved in ignition through transition to flame spread. Such a model is used in this paper [1] and differs from the traditional approach in which limiting conditions are based on the limits of steady flame spread. At a sufficiently low external wind speed, transition fails to occur and the flame is quenched due to insufficient oxygen and radiative heat losses [2]. The processes involved in this quenching limit cannot be studied in normal gravity because buoyancy-induced flow provides sufficient oxygen for flame transition to occur.

The focus of this paper is to investigate the influence of flame geometry on the likelihood of transition from ignition to flame spread in near-quenching conditions. This can be done by simulating the ignition and possible transition to flame spread on a thermally thin solid in the presence of an imposed wind. Pyrolysis of the solid is initiated by applying an external radiative flux to the central region of the solid. The spatial distribution of this radiative flux on the solid is either circular or linear, which gives rise to two different flame shapes. For the wind velocity range considered here, flame spread occurs in the upwind direction [3]. Conditions that are near quenching, due to insufficient oxygen, are identified by varying the wind speed.

Theoretical Model

Since the theoretical model used for the condensed-phase sample has been described in Ref. [4], only a summary will be given here. A global approach is used to define both the gas-phase oxidation reaction and the thermal degradation reactions of the condensed phase. Although more detailed kinetic modeling is possible, the numerical solution of the resulting system of equations would be prohibitively expensive. The thermal degradation of the sample is modeled by three exothermic global reactions governing pyrolysis (slightly exothermic), thermal oxidation, and char oxidation. The evolution of the thermal degradation process is governed by conservation equations for solid mass, cellulose, char, and energy with Arrhenius-type reaction rates [5]. The global kinetic constants and heats of reaction were obtained by thermogravimetric analysis and are identical to those used in Ref. [1]. As reported in Ref. [3], the sample's thickness is 0.13 mm; area density is 5.7 mg/cm^2; specific heat is 0.96 J/(g · K); emissivity is 0.6. The specific heat increases linearly with temperature and is also used for the

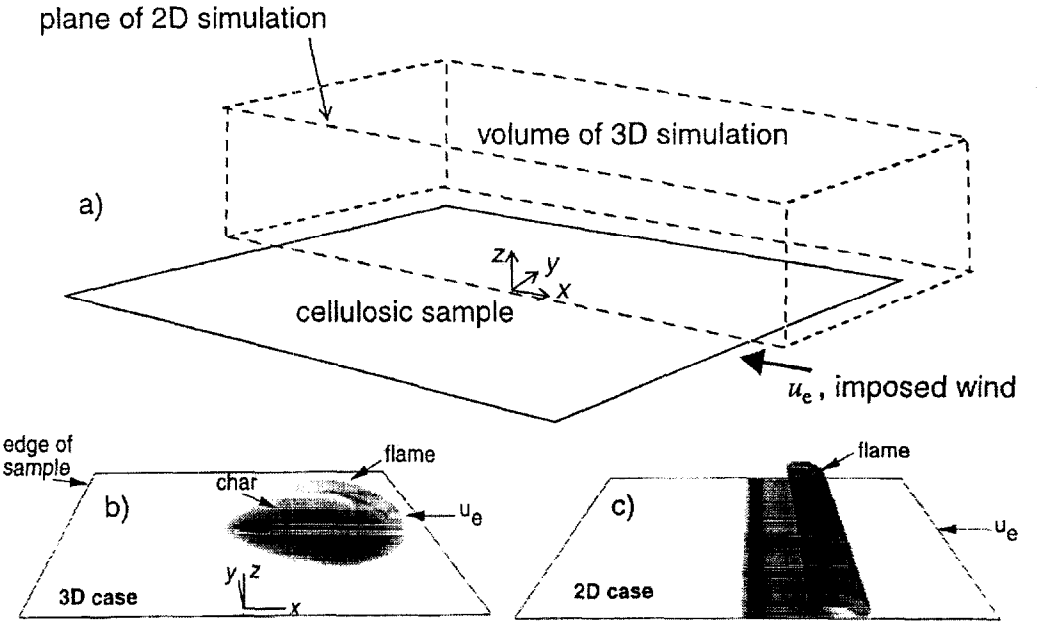

FIG. 1. (a) Schematic showing the cellulosic sample and computational domains of the 2- and 3-D simulations. Horizontal dimensions of sample are 10 cm × 10 cm. The 3-D simulation (10 cm × 5 cm × 4.8 cm) includes half the width and thickness of the sample. The 2-D simulation domain is the $y = 0$ plane. (b) and (c) show characteristic char patterns on the sample surface and iso-surfaces of the gas-phase reaction rate [5×10^{-5} g/(cm$^3 \cdot$ s)] from the 3-D and 2-D simulations, respectively. Ambient oxygen mass fraction is 0.33 and $u_e = 2$ cm/s. The area covered by the radiant flux ignition source (darkest char regions) is circular in the 3-D simulations and planar in the 2-D simulations.

char and cellulose [6]. The sample is assumed to be thermally thin and of uniform composition with depth. Radiative losses from the surface are included.

The gas-phase model [5] consists of the conservation equations for total mass, momentum (full Navier-Stokes), energy, and species mass fractions (fuel and oxygen) formulated in the low Mach number limit. A global one-step reaction

$$[\text{Fuel Gas}] + \nu_{O_2}\,[\text{Oxygen}] \rightarrow \text{Product} \quad (1)$$

with an Arrhenius rate is used. The preexponential factor in the reaction rate is 5.0×10^9 cm^3/(g $\cdot$ s); the activation energy is 67 kJ/mol; the heat of combustion is 35 kJ/g; and the stoichiometric constant is $\nu_{O_2} = 3.57$. The values are identical to those used in previous two-dimensional (2-D) [3] and three-dimensional (3-D) [1] studies. Unlike the condensed-phase kinetic constants, the gas-phase constants are not experimentally measured. Ignition and transition to flame spread have been found to be very sensitive to the values used for the gas-phase kinetic constants. With the values used here, simulated and experimental [7] flame spread rates were in approximate agreement. The average molecular weight is assumed to be constant; temperature-dependent molecular transport coefficients are used. All gases have equal mass diffusivity, which is not necessarily equal to the thermal diffusivity. Ignition is initiated by an external radiative flux on the sample surface. Radiative emission and absorption in the gas is not included.

Zero gradient boundary conditions are used for the far-field values of the mass fractions and temperature, which decay exponentially with distance from the flame. The velocity potential decays algebraically from the heated region [5]. Far-field velocity boundary conditions, therefore, are obtained from the analytically determined velocity potential, which depends on the mass flux and heat transfer at the sample surface [5]. The domain is open to the ambient environment, which results in a constant thermodynamic pressure.

Numerical Model

The numerical model has been described in Ref. [1]. Both 2- and 3-D simulations were performed. A sketch of the cellulosic sample and the simulation domains is shown in Fig. 1a. The domain for the 2-D simulations consists of the $y = 0$ (centerline) plane. The darkest char regions of Figs. 1b and 1c show the spatial distribution of the external radiative flux used for ignition. The governing equations for the condensed phase are solved using a stiff ordinary differential equation solver. A finite difference control volume approach on a staggered grid is used to solve the gas-phase equations. A time-splitting algorithm is used for the species and temperature

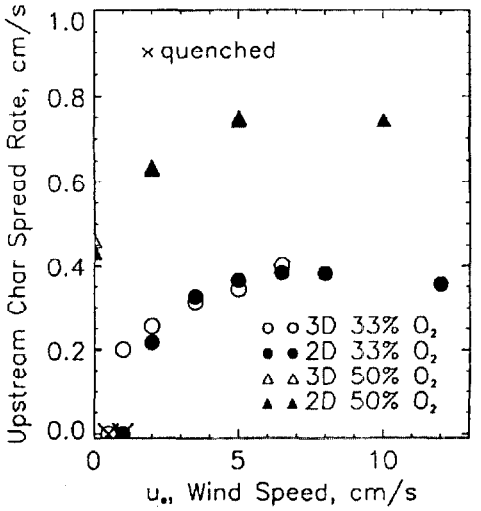

FIG. 2. Upstream char spread rate versus the speed of the imposed wind.

equations because the characteristic time scale of the chemical reaction is relatively small compared with that for diffusion and convection (high Damköhler number) [5]. This method involves first solving the species and temperature equations without the convective and diffusive terms, using a stiff ordinary differential equation solver over small time steps. The global time stepping is performed using an alternating direction implicit (ADI) scheme on the convective and diffusive terms. The momentum equation is solved using a projection method; the solution to the Poisson equation for the pressure perturbation is found with a direct solver.

The numerical grid is uniform in the horizontal directions and stretched in the vertical. Cell sizes are 0.66 mm in the horizontal directions (parallel with the sample), start at 0.25 mm at the sample surface, and stretch to 2 mm at the top of the computational domain. Various grid resolutions were used to ensure grid independence of the results (e.g., flame spread rates, quenching conditions). The physical dimensions of the 3-D computational domain are 12.8 cm × 6.4 cm × 4.8 cm in the x, y, and z direction, respectively (12.8 cm × 4.8 cm for 2-D); the sample size in the 3-D simulations is 10 cm × 5 cm. A typical 3-D grid contains about 600,000 grid points (192 × 96 × 32). For the 3-D runs, approximately 24 h CPU time are needed for 1.5 s of simulated real time on current generation workstations.

Results

In all simulations the sample is ignited with a radiant flux that approximates that used in experiments. This flux decays exponentially with distance from the center of the sample as $\exp[-(x/h)^2]$ in the 2-D [Fig. 1c] case and $\exp[-\{(x/h)^2 + (y/h)^2\}]$ in the 3-D [Fig. 1b] case. The half-width of the profile is $h = 0.25$ cm. The flux ramps up in time following $\tanh[t/(0.75\text{ s})]$; at $t = 3.5$ s it is set to zero. Convective oxygen supply to the flame is controlled by varying the magnitude of the imposed wind u_e (see Fig. 1). Figs. 1b and 1c show the characteristic shape of the 3-D and 2-D flames and the degree and pattern of char on the sample surface for a well-established flame. For better visualization the 3-D data have been reflected across the $y = 0$ symmetry plane; the 2-D data have been extended in along the positive y axis and then reflected across $y = 0$. The wind speed is $u_e = 2$ cm/s and the ambient oxygen mass fraction value is $Y_O^\infty = 0.33$. The flame spreads in the upwind direction only in both cases, which is consistent with experimental results in a $Y_O^\infty = 0.35$ atmosphere. Three-dimensional simulations using the 2-D radiant flux were performed to ensure that no important 3-D effects developed which could not be captured by a fully 2-D simulation.

Figure 2 shows the upstream flame spread rate versus u_e from 2-D and 3-D simulations in atmospheres of $Y_O^\infty = 0.33$ and 0.5. The spread rate was determined by a linear fit to the upstream movement of the $Y_{char} = 0.1$ level of the char mass fraction on the sample surface at the centerline. The trend of increasing spread rate with u_e (for u_e less than approximately 5 cm/s) followed by a relatively constant spread rate for larger u_e is consistent with experimental results [7,8]. None of the flames in the $Y_O^\infty = 0.5$ case were quenched, even in the absence of an imposed wind. Quenching does occur in both the 2-D and 3-D simulations when the ambient oxygen is lowered to $Y_O^\infty = 0.33$. The 2-D case quenches at a larger u_e value than the 3-D case. These results imply that $u_e \approx 0.5$ cm/s for the 3-D flame and $u_e \approx 1$ cm/s for the 2-D flame are near the quenching limit due to insufficient oxygen supply. Next, 2-D and 3-D results for $u_e = 1$ cm/s will be compared to better understand why the 3-D flame survives at smaller u_e.

Figures 3a and 3b show centerline ($y = 0$) profiles (2-D and 3-D cases, respectively) of the net heat flux on the sample surface (q_s, black lines), the conductive/convective heat flux ($q_c = -k\nabla T \cdot \mathbf{n}$, red lines), and the height at which the maximum temperature occurs (solid circles). Here k is the thermal conductivity, T the temperature, and $\mathbf{n}$ the unit normal on the sample surface pointing out of the computational domain. Above the centerline profiles are color contours of the reaction rate, oxygen (black) and fuel (red) mass flux vectors, and velocity streamlines. The fuel mass flux, which is similar in the 2-D and 3-D case, is not shown in Fig. 3b for visual clarity. These data are at time $t = 1.5$ s for the $u_e = 1$ cm/s case; the ambient wind flows from right to left. This time is chosen because it is after ignition and is characteristic of times up to $t = 3.5$ s when the external radiant flux stops. The external radiant heat flux, the

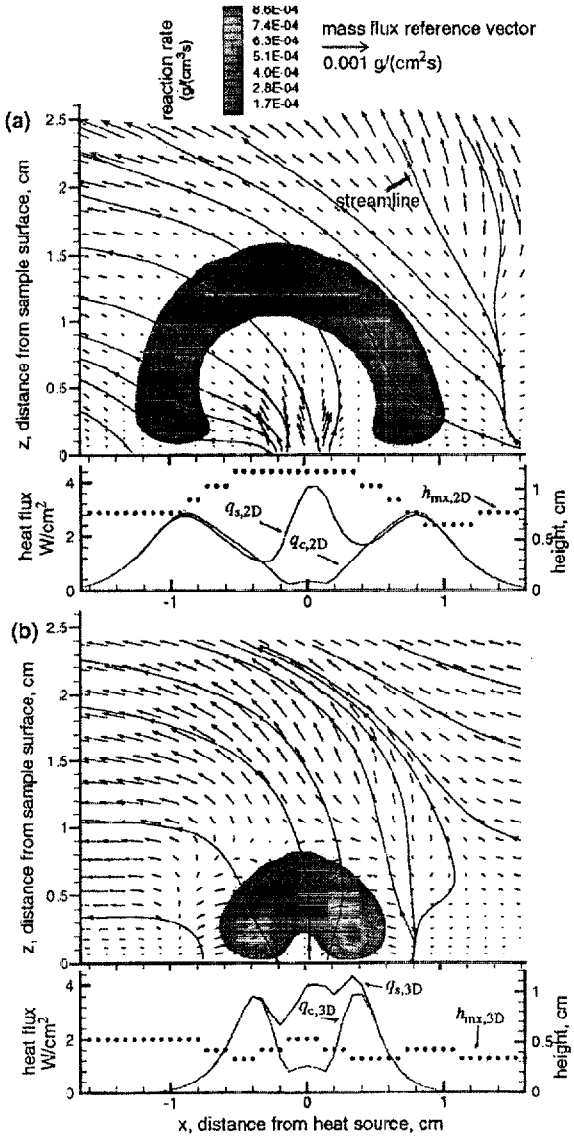

FIG. 3. Results of the (a) 2-D and (b) 3-D case with u_e = 1 cm/s at t = 1.5 s. The base of each figure has centerline (y = 0) profiles of the net heat flux, q_s, (black line) and the heat flux from conduction/convection, q_c, (red line) on the sample surface. The height at which the maximum temperature occurs, h_{mx}, is also shown with black circles. Above the centerline profiles are color contours of the gas-phase reaction rate in the x-z plane. Fuel [red arrows, in (a) only] and oxygen (black arrows) mass flux vectors along with velocity streamlines are also plotted. The reference vector corresponds to a mass flux magnitude of $|\dot{\mathbf{m}}''|$ = 0.001 g/(cm² · s) for both the fuel and oxygen.

three exothermic reactions of the sample degradation and thermal conduction from the hot products of the gas-phase reaction all contribute to heat flux into the sample. Radiative cooling is the only source of heat flux away from the sample surface. The net surface heat flux in both the 3-D ($q_{s,3\text{-D}}$) and 2-D ($q_{s,2\text{-D}}$) simulations is triple peaked. The center peak, at x = 0, is the symmetry point of the external heat flux and the center of the pyrolysis region as can be seen in Fig. 3a. The $q_{s,3\text{-D}}$ and $q_{s,2\text{-D}}$ fluxes are in agreement near x = 0 where the external radiant flux dominates. Mixing of the fuel and oxygen occurs at the sides, away from x = 0. As a result, away from x = 0, q_s becomes dominated by heat transfer from the hot gases produced from the gas-phase reaction ($q_s \approx q_c = k\ \partial T/\partial z$). The $q_{s,3\text{-D}}$ side peaks are significantly larger and closer to the center than in the 2-D case. The same is true for the reaction rates.

The maximum temperatures (not plotted) were found to be larger in the 2-D case. At first this seems inconsistent with the q_s data in Fig. 3, which shows that the side peaks of $q_{s,3\text{-D}}$ (which are dominated by $-k\nabla T \cdot \mathbf{n}$) are significantly larger than $q_{s,2\text{-D}}$. However, the values of $h_{mx,3\text{-D}}$ and $h_{mx,2\text{-D}}$ (the height of the maximum temperature) in Fig. 3 show that the $q_{s,3\text{-D}}$ side peaks are larger than $q_{s,2\text{-D}}$ because the maximum temperatures in the 3-D case occur closer to the sample surface (h_{mx} has a steplike behavior because it can only equal the discrete values defined by the computational grid).

The presence of smaller peak temperatures located closer to the sample surface and larger gas-phase reaction rates suggest that the diffusion of oxygen to the flame in the centerline plane is stronger in the 3-D case. If more oxygen is present near the sample surface due to diffusion, then fuel and oxygen will mix more fully and react at lower heights. This view is supported by comparing the velocity streamlines and the vectors of oxygen mass flux

$$\dot{\mathbf{m}}''_O = \rho \mathbf{u} Y_O - \rho D \nabla Y_O \qquad (2)$$

Here ρ is the density of the gas, D is the diffusivity and $\mathbf{u}$ the velocity vector. Note that diffusive transport (the second term on the right-hand side of equation 2) dominates convective transport (the first term) in locations where the mass flux vectors and streamlines do not point in the same direction. It is clear from comparison of Figs. 3a and 3b that significantly more oxygen diffusion to the flame occurs in the 3-D case. Oxygen mass flux vectors near and within the flame (as located by the reaction rate contours) are perpendicular or even nearly antiparallel to the streamlines.

Figure 4 shows the streamlines and mass flux vectors for both the oxygen and fuel in the x-y plane at a height of z = 2.5 mm for the same external wind (u_e = 1 cm/s) and time (t = 1.5 s) values used in Fig. 3. The upper and lower halves of the figure contain the fuel and oxygen mass flux vectors, respectively. Pyrolysis and expansion from the gas-phase reaction create an obstacle that the upstream originating flow circumvents, as can also be seen in Fig. 3. Fuel gases flow radially from the center due to diffusion and expansion. As in Fig. 3b, far from

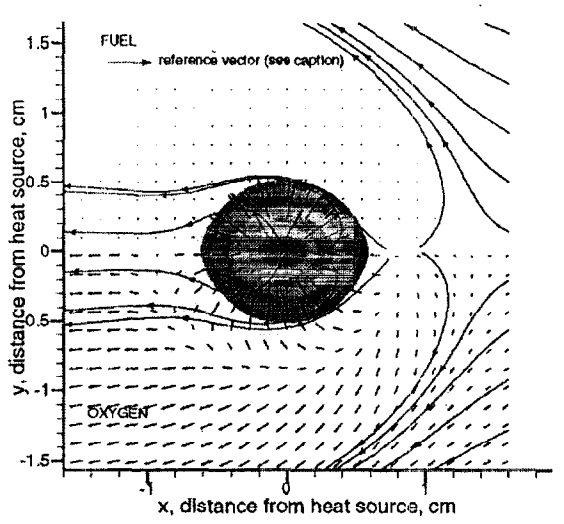

FIG. 4. Results of the 3-D, u_e = 1 cm/s run at t = 1.5 s on the x-y plane of height z = 2.5 mm. The upper half of the figures contains fuel mass flux vectors; the lower half contains oxygen mass flux vectors. The reference vector corresponds to a $|\dot{m}''_F|$ = 0.00025 g/(cm^2·s) for the fuel and $|\dot{m}''_O|$ = 0.001 g/(cm^2·s) for the oxygen ($\dot{m}''$ is the mass flux vector). Velocity streamlines and reaction rate color contours are also shown. The legend for the reaction rate levels is on Fig. 3.

the flame the oxygen mass flux vectors and streamlines point in the same direction (convective flux dominates). Oxygen mass flux along the outer regions of the flame (i.e., along outer reaction rate contours) is toward the centerline plane. Near the center of the flame, the oxygen mass flux vectors and streamline directions are opposite; the magnitude of the flux from the side is nearly equal to the centerline flux in the upstream part of the flame. Diffusion in the 2-D case can only occur within the centerline plane. Thus, it is clear that the curvature in the x-y plane of the 3-D flame allows more oxygen to diffuse to the center of the flame. The 3-D flame is therefore less dependent on oxygen supply from an external wind and successfully undergoes transition to flame spread while the 2-D flame is quenched.

As time proceeds, the 3-D flame grows in the cross-stream direction and the curvature in the x-y plane near the centerline decreases as can be seen in Fig. 5 and Fig. 6. The 2-D and 3-D heat flux centerline profiles, reaction rate contours, mass flux vectors, and streamlines plotted previously in Fig. 3 for t = 1.5 s and u_e = 1 cm/s are repeated in Fig. 7 for t = 10 s and u_e = 2 cm/s. This flame is well past transition. Compared with Fig. 3, the 2-D and 3-D flames are much more similar in shape, size, and peak reaction rate. The surface flux is larger in the

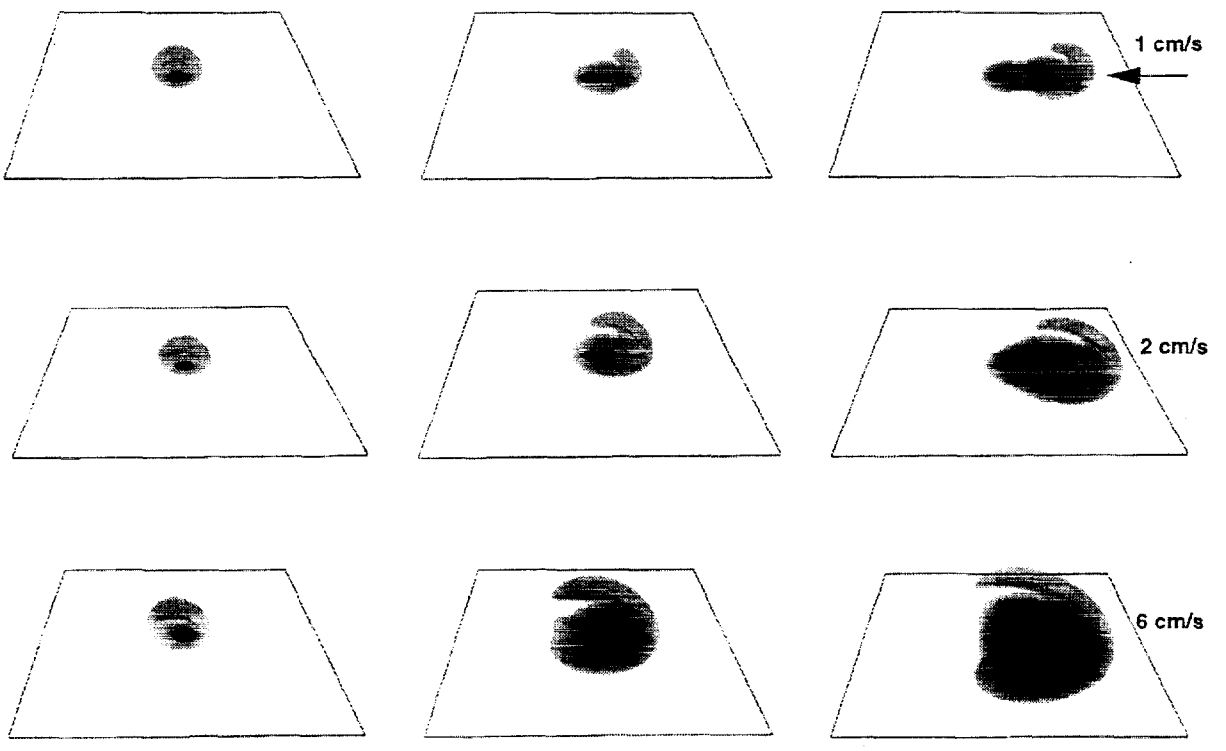

FIG. 5. Time development of the 3-D flame for three different wind speeds, u_e = 1 cm/s, 2 cm/s and 6 cm/s. Both the gas-phase reaction rate isosurface [5 × 10^{-5} g/(cm^3·s)] and greyscale contours of the char mass fraction on the sample surface are shown. The darker region corresponds to a higher char mass fraction. The 1 cm/s case is shown at t = 4 s, 10 s, 21 s; the 2 cm/s case at t = 4 s, 10 s, 20 s; the 6 cm/s at t = 4 s, 9 s, 14 s.

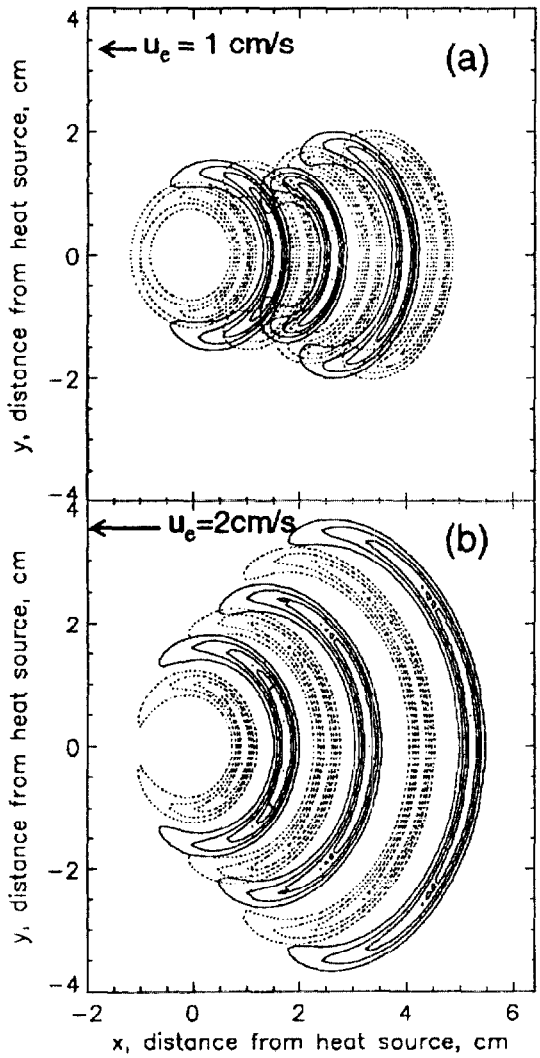

FIG. 6. Time sequence of contour plots of the reaction rate in the x-y plane at a height of z = 1.2 mm for (a) u_e = 1 cm/s and (b) 2 cm/s runs. Both figures start at t = 4 s; successive contour plots are separated by 3 s. Contour line formats alternate between solid lines and dotted lines so successive times can be more easily distinguished.

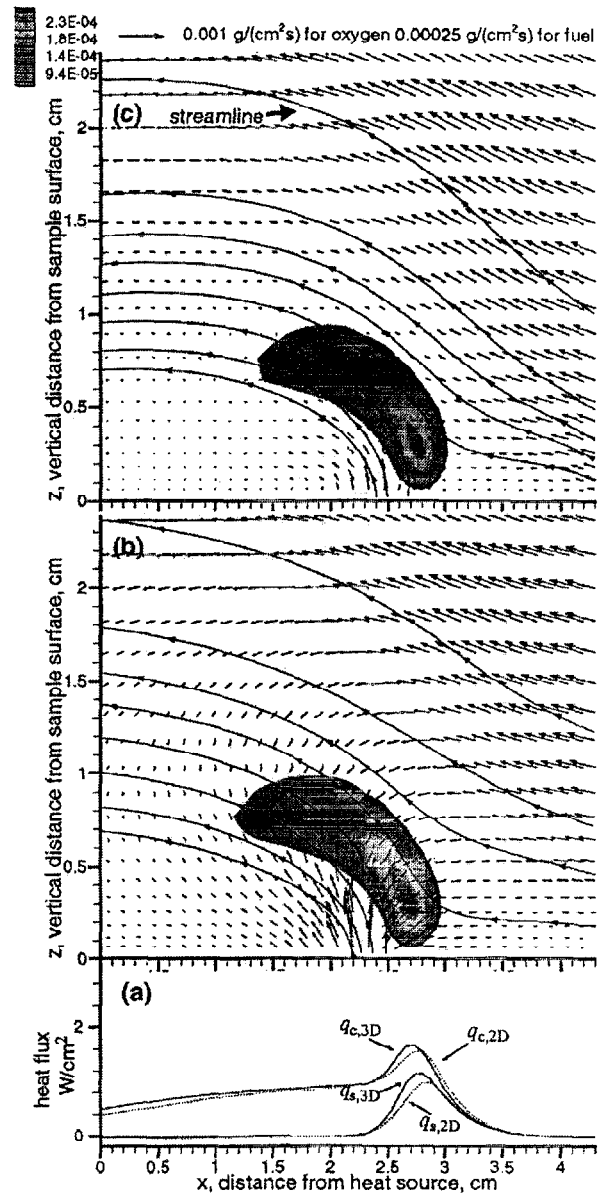

FIG. 7. Results of the 2-D and 3-D case with u_e = 2 cm/s at t = 10 s. (a) Shows centerline (y = 0) profiles of the net heat flux, q_s (solid black line for 3-D, dotted black line for 2-D), and the heat flux from conduction/convection, q_c (solid red line for 3-D, dotted red line for 2-D) on the sample surface. Above the centerline profiles are color contours of the gas-phase reaction rate in the x-z plane for the (b) 3-D and (c) 2-D case. Fuel (red arrows) and oxygen (black arrows) mass flux vectors along with velocity streamlines are also plotted. The reference vector shown at the top of the figure corresponds to a mass flux magnitude of $|\dot{m}''_F|$ = 0.001 g/(cm^2·s) for the oxygen and $|\dot{m}''_O|$ = 0.00025 g/(cm^2·s) for the fuel.

3-D case (Fig. 7b), which results in greater fuel pyrolysis and a 15% greater rate of flame spread as measured by char levels (Fig. 2). Similar to Fig. 3b, the magnitude of the oxygen mass flux vectors in and near the flame is larger in the 3-D case and, except at the base of the leading edge, dominated by diffusion. As a result, the peak reaction rate region is relatively extended. Note that the magnitude of the oxygen mass flux in the area of peak reaction rate in Fig. 7b is smaller than in the 3-D flame of Fig. 3b, which has more curvature.

Figures 5 and 6 show the development of the 3-D flame over time for various u_e cases. It is clear from Fig. 6a that for u_e = 1 cm/s, the flame first grows in the cross-stream direction, then shrinks (weakens) to a minimum size at t = 13 s (fourth

contoured flame), and then grows again before apparently stabilizing (the simulation was halted because the end of the sample was reached). The flame in the 2 cm/s and 6 cm/s cases grows monotonically (most clearly seen in Fig. 6b for the 2 cm/s). Note that while the flame shrinks and then grows (Fig. 6a) the paper surface under the cross-stream extremities (wings) of the flame is subjected to prolonged heat flux compared with the centerline. From $t = 7$ s to 1.6 s reaction rate contours can be seen to overlie a region centered at approximately $x = 1.5$ cm, $y = 1$ cm. This causes significant charring under the wings of the flame as can be seen in Fig. 5. As the flame size decreases, the curvature of the flame increases and oxygen mass flux from the wings of the flame is more and more toward the flame's center. In the $u_e = 1$ cm/s case this process eventually leads to a stronger flame. This process could not occur in the 2-D flames of this study.

Conclusions

By varying the magnitude of the imposed wind, u_e, it was found that the 2-D flame quenched (from lack of oxygen) more easily (i.e., at larger values of u_e) than the 3-D flame. A $u_e \approx 1$ cm/s value was near the quenching limit for the 2-D case. During transition with $u_e = 1$ cm/s, the 3-D flame (along the centerline) was closer to the surface of the cellulosic sample compared to the 2-D flame. As a result, heat flux to the sample surface, and the resulting pyrolysis, was greater in the 3-D case. Significant diffusion of oxygen from the sides (in a direction perpendicular to the imposed wind) to the centerline plane occurred in the 3-D case. Oxygen supply to the 2-D flame could only occur within the centerline plane. It is likely that this increased diffusion of oxygen in the 3-D flame caused the fuel to mix with oxygen at lower heights, resulting in a flame that is closer to the sample surface. The 3-D flame, therefore, required less oxygen supply from an external wind to undergo transition to flame spread. Once flame spread was established there was little difference between the 3-D (centerline plane) and 2-D flames due to the decreased curvature of the 3-D flame in the x-y plane (relative to the curvature during ignition and transition). Further experimentation is needed to validate these results.

Acknowledgments

This work is funded by the NASA Microgravity Science Program under the Inter-Agency Agreement No. C-32001-R under technical monitor Dr. Sandra Olson. The authors would like to thank Dr. Kevin McGrattan for providing the simulation code used in this study.

REFERENCES

1. Kashiwagi, T., McGrattan, K. B., Olson, S. L., Fujita, O., Kikuchi, M., and Ito, K., in *Twenty-Sixth Symposium (International) on Combustion*. The Combustion Institute, Pittsburgh, 1996, pp. 1345–1352.
2. di Blasi, C., *Combust. Flame* 100:332–340 (1995).
3. McGrattan, K. B., Kashiwagi, T., Baum, H. R., and Olson, S. L., *Combust. Flame* 106:377–391 (1996).
4. Kashiwagi, T. and Nambu, H., *Combust. Flame* 88:345–368 (1992).
5. Nakabe, K., McGrattan, K. B., Kashiwagi, T., Baum, H. R., Yamashita, H., and Kushida, G., *Combust. Flame* 98:361–374 (1994).
6. Milosavljevic, I., "Behavior of Charring Materials in Simulated Fire Environment," Ph.D. thesis, Division of Engineering, Brown University, 1994.
7. Olson, S. L., *Combust. Sci. Technol.* 76:233–249 (1991).
8. Kashiwagi, T., Mell, W. E., McGrattan, K. B., Baum, H. R., Olson, S. L., Fujita, O., Kikuchi, M., and Kenichi, I., *Proceedings of Fourth International Microgravity Combustion Workshop*, Cleveland, OH, May 19–21, 1997.